Geophysical Journal International

Geophys. J. Int. (2022) **228,** 193–212
Advance Access publication 2021 August 04
GJI Marine Geosciences and Applied Geophysics

https://doi.org/10.1093/gji/ggab296

One year of sound recorded by a MERMAID float in the Pacific: hydroacoustic earthquake signals and infrasonic ambient noise

Sirawich Pipatprathanporn and Frederik J. Simons

Department of Geosciences, Princeton University, Princeton, NJ 08544*, USA. E-mail: sirawich@princeton.edu*

Accepted 2021 August 2. Received 2021 July 7; in original form 2021 March 30

SUMMARY

A fleet of autonomously drifting profiling floats equipped with hydrophones, known by their acronym MERMAID, monitors worldwide seismic activity from inside the oceans. The instruments are programmed to detect and transmit acoustic pressure conversions from teleseismic *P* wave arrivals for use in mantle tomography. Reporting seismograms in near-real time, within hours or days after they were recorded, the instruments are not usually recovered, but if and when they are, their memory buffers can be read out. We present a unique 1-yr-long data set of sound recorded at frequencies between 0.1 and 20 Hz in the South Pacific around French Polynesia by a MERMAID float that was, in fact, recovered. Using time-domain, frequency-domain and time-frequency-domain techniques to comb through the time-series, we identified signals from 213 global earthquakes known to published catalogues, with magnitudes 4.6–8.0, and at epicentral distances between 24° and 168°. The observed signals contain seismoacoustic conversions of compressional and shear waves travelling through crust, mantle and core, including *P*, *S*, *Pdif*, *Sdif*, *PKIKP*, *SKIKS*, surface waves and hydroacoustic *T* phases. Only 10 earthquake records had been automatically reported by the instrument—the others were deemed low-priority by the onboard processing algorithm. After removing all seismic signals from the record, and also those from other transient, dominantly non-seismic, sources, we are left with the infrasonic ambient noise field recorded at 1500 m depth. We relate the temporally varying noise spectral density to a time-resolved ocean-wave model, WAVEWATCH III. The noise record is extremely well explained, both in spectral shape and in temporal variability, by the interaction of oceanic surface gravity waves. These produce secondary microseisms at acoustic frequencies between 0.1 and 1 Hz according to the well-known frequency-doubling mechanism.

Key words: Pacific Ocean; Seismic noise; Infrasound.

1 INTRODUCTION

Global seismic tomography, the imaging of 3-D wave speed structure inside the Earth (Ritsema & Lekić 2020; Tromp 2020), is data-limited by the sparsity of oceanic stations (Romanowicz 2008). Approaches to mitigate this problem include installing moored hydrophones (e.g. Fox *et al*. 1993) and ocean bottom seismometers (e.g. Stephen *et al*. 2003). The logistical difficulties and high costs of installation and data recovery of these devices render such methods not viable for filling vast gaps in the ocean with sufficient station density for seismic tomography. Repurposing ocean-bottom telecommunication optic fibers for distributed acoustic sensing (e.g. Marra *et al*. 2018) may hold promise for extending the range of existing seismic arrays (e.g. Williams *et al*. 2019). MERMAID (Mobile Earthquake Recording in Marine Areas by Independent Divers) is a more established recent alternative (Simons *et al*. 2006b; Sukhovich *et al*. 2015; Simon *et al*. 2020, 2021a). This low-cost, easily deployable and generally unrecovered robotic instrument is capable of maintaining a constant depth in the ocean, where it continuously records the acoustic pressure field, and autonomously reports seismoacoustic waveform arrivals in near-real time. A combination of time-domain triggering and probabilistic wavelet-domain identification algorithms (Simons *et al*. 2006a; Sukhovich *et al*. 2011) running onboard determines detections of likely teleseismic earthquake *P*-wave arrivals, prompting MERMAID to surface and report the recorded waveforms via satellite before resuming its mission.

Over the last decade, multiple generations of MERMAID instruments have collected thousands of earthquake signals recorded in the oceans, suitable for seismic tomography and more (Simons *et al*. 2009; Sukhovich *et al*. 2015; Nolet *et al*. 2019; Simon *et al*. 2021b). Nevertheless, the bulk of the acoustic record never gets transmitted but remains in the instrument's memory, which, in the third

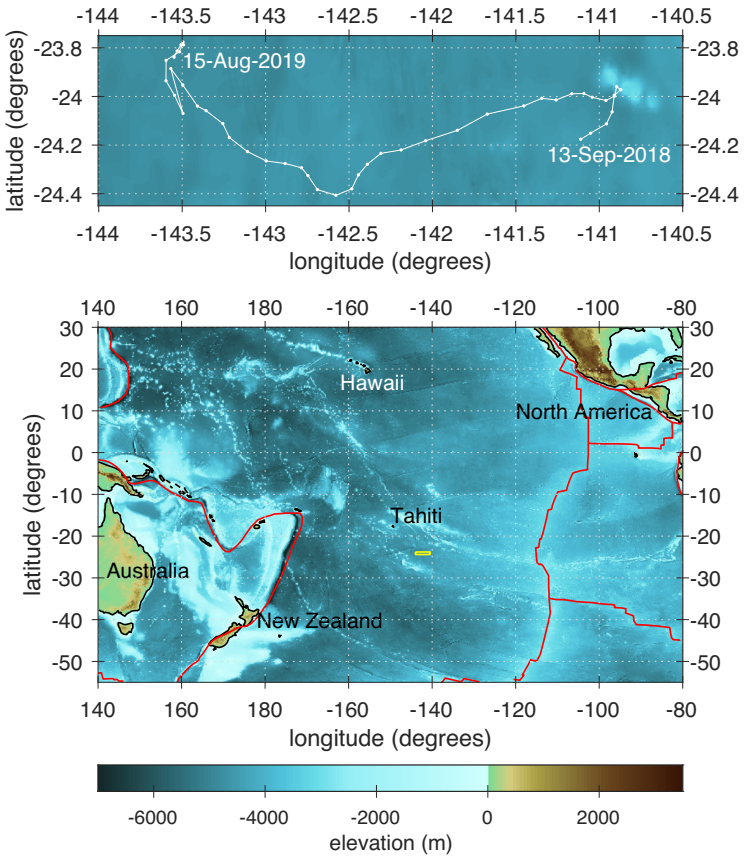

Figure 1. Top panel: trajectory of MERMAID P0023 from its launch on 13 September 2018 to its recovery on 15 August 2019. Each dot is a different, approximately weekly, surfacing. Connecting lines do not take into account the complexities of the currents at depth. Bottom panel: bathymetry and topography of the area of the Pacific centred on French Polynesia. Coastlines are drawn in black, plate boundaries in red. The yellow rectangle identifies the upper panel.

MERMAID generation (Hello & Nolet 2020; Simons *et al*. 2021), holds 1 yr of data. The memory buffer might contain unreported earthquakes, undetected earthquakes and noise from a variety of terrestrial, oceanic and biological sources. We do note that frequencies above 20 Hz are filtered out by the acquisition module, which effectively avoids whale vocalizations—future versions of MERMAID instruments may well be designed to specifically capture those (Bonnieux *et al*. 2020). In principle, all such data can be recovered, as MERMAID's current satellite protocol provides for two-way communication that allows for data requests (Simon *et al*. 2021b). The MERMAID instrument itself is not meant to be recovered, unless special circumstances permit. Exceptionally, during a cruise leg of the South Pacific Plume Imaging and Modeling (SPPIM) experiment conducted in August 2019, Princeton University's instrument P0023 was recovered and redeployed, allowing for the repatriation of a 1-yr time-series.

Working in the time-domain (raw seismograms), in the time-frequency domain (spectrograms), and in the spectral domain (power-spectral densities), we mined the data set for signal and noise. We first identified all possible earthquake arrivals in the buffer and then matched them, to the extent possible, with known earthquakes from the United States Geological Survey (USGS) National Earthquake Information Center (NEIC) Preliminary Determination of Epicenters (PDE) database, accessed via the Incorporated Research Institutions for Seismology (IRIS) Data Management Center (DMC). In total 213 wave arrivals were matched in this way. Only 10 of those had already been transmitted by MERMAID.

We removed all identified and suspected seismoacoustic (e.g. *P*, *S* and surface wave conversions) and transient hydroacoustic arrivals (e.g. *T* phases) from the record to obtain the background noise. We computed the noise spectral density over yearly, monthly and weekly intervals to study its fluctuation over the year. Our data rather directly confirm that the ocean surface is responsible for the infrasonic ambient noise at 1500 m depth through the secondary-microseism generating process which creates seismic energy at double the driving frequency (see Kerman 1993; Nakata *et al*. 2019, and references therein). Our *in situ* observations of acoustic noise in the 0.1–1.0 Hz frequency range are remarkably coherent with sea-surface pressure obtained from completely independent ocean gravity wave modelling (WAVEWATCH III, Tolman 2009).

Our study highlights the promise for recording and recovery of seismic phases beyond the most prominent automatically reported ones (see also Simon *et al*. 2021b), and illustrates the potential of MERMAID as an environmental low-frequency ambient-noise sensor.

2 DATA AND METHODS

Our data are time-domain records of acoustic pressure acquired by MERMAID P0023 at a parking depth of 1500 m below the ocean surface in Pacific French Polynesia between its first deployment on 13 September 2018 and its fortuitous recovery on 15 August 2019. Their nominal sampling rate is 40 Hz, corresponding to a Nyquist frequency of 20 Hz. The hydrophone has approximately linear sensitivity to pressure down to about 0.1 Hz, with a (negative!) scaling

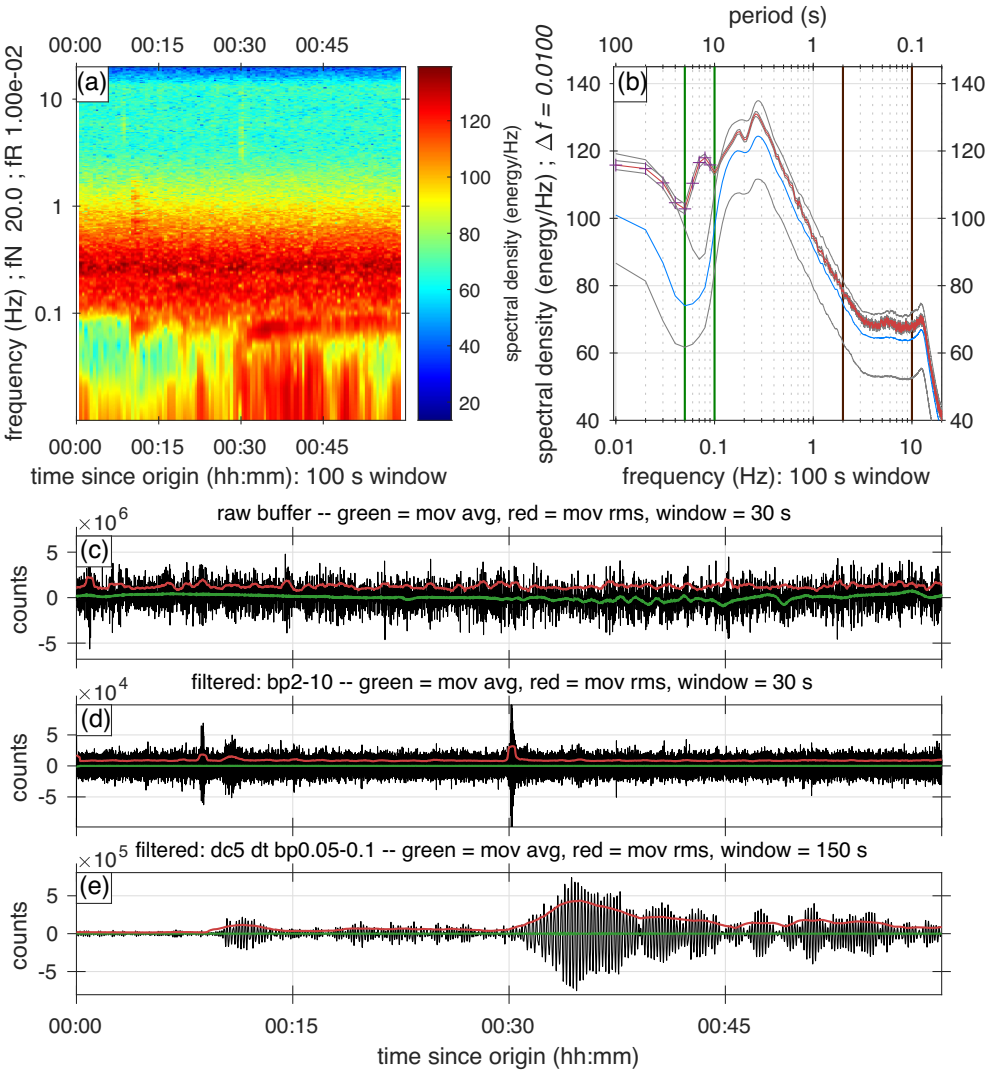

Figure 2. One hour of acoustic pressure data from the recovered MERMAID P0023 buffer, in uncalibrated instrument counts. The interval contains the signal from a magnitude 6.7 earthquake near the coast of Coquimbo, Chile on 20 January 2019 at 01:32:52.480 UTC. (a) Spectrogram showing seismic arrivals most prominently in the 0.08–0.10 Hz frequency band. (b) Spectral density of the data in (a), shown in red with grey uncertainty intervals, compared to the noise spectral density representative of the entire month of January 2019, in blue with grey uncertainties. Both curves differ most at frequencies below 0.10 Hz. (c) Time-domain raw seismogram. (d) Seismogram filtered between 2 and 10 Hz. (e) Seismogram filtered between 0.05 and 0.10 Hz. Green and red lines in (c)–(e) are moving averages and moving rms values.

factor of -1.494×10^5 counts Pa^{-1}. A transfer function (Guust Nolet, Olivier Gerbaud and Frédéric Rocca, personal communication, see also Joubert *et al*. 2015) is on record at and available from the IRIS DMC. The incoming data stream is filtered between 0.1 and 10 Hz before digitization.

In-between surfacings, which take about 22 hr round-trip (Simon *et al*. 2021a) and during which recording is halted, the time-series is continuous except for sporadic intervals of depth adjustments, which interrupt data acquisition for a few minutes each. MERMAID returns to the surface as soon as it deems a detected *P*-wave arrival likely to be of use for seismic tomography, which occurs on average every 6–7 d. At this rate of data return, the lifetime of a MERMAID instrument on a single set of lithium batteries is about 5 yr.

At the time of data transmission, Global Positioning System (GPS) location and time are obtained and bundled as metadata. The GPS time stamp is used to correct for instrument clock drift (Joubert *et al*. 2016), typically by a fraction of a second (Simon *et al*. 2021a). Over the course of the 11-month (about 336 d, or 8064 hr) period discussed here, MERMAID surfaced 44 times. In total, we have 7029 hr of data available, an 'uptime' equivalent of 87 per cent of the deployed time.

Fig. 1 shows the instrument's trajectory over the period discussed in this paper. In the figure lines are drawn to connect surface locations, but when time-tagging particular events in the seismograms recorded at depth, a more sophisticated procedure is being followed, which takes into account the difference in drift rate between the surface and the usually 1500 m parking depth (Joubert *et al*. 2016). Examples and details of drift statistics are given by Nolet *et al*. (2019) and Simon *et al*. (2021a).

We analyse the data in the time-frequency domain, in the frequency domain and in the time-domain, in various frequency bands. The choice of corner frequencies arose from visual inspection of spectrograms and spectral densities (Simons *et al*. 2009), and with an eye towards identifying earthquake signatures (seismoacoustic *P*

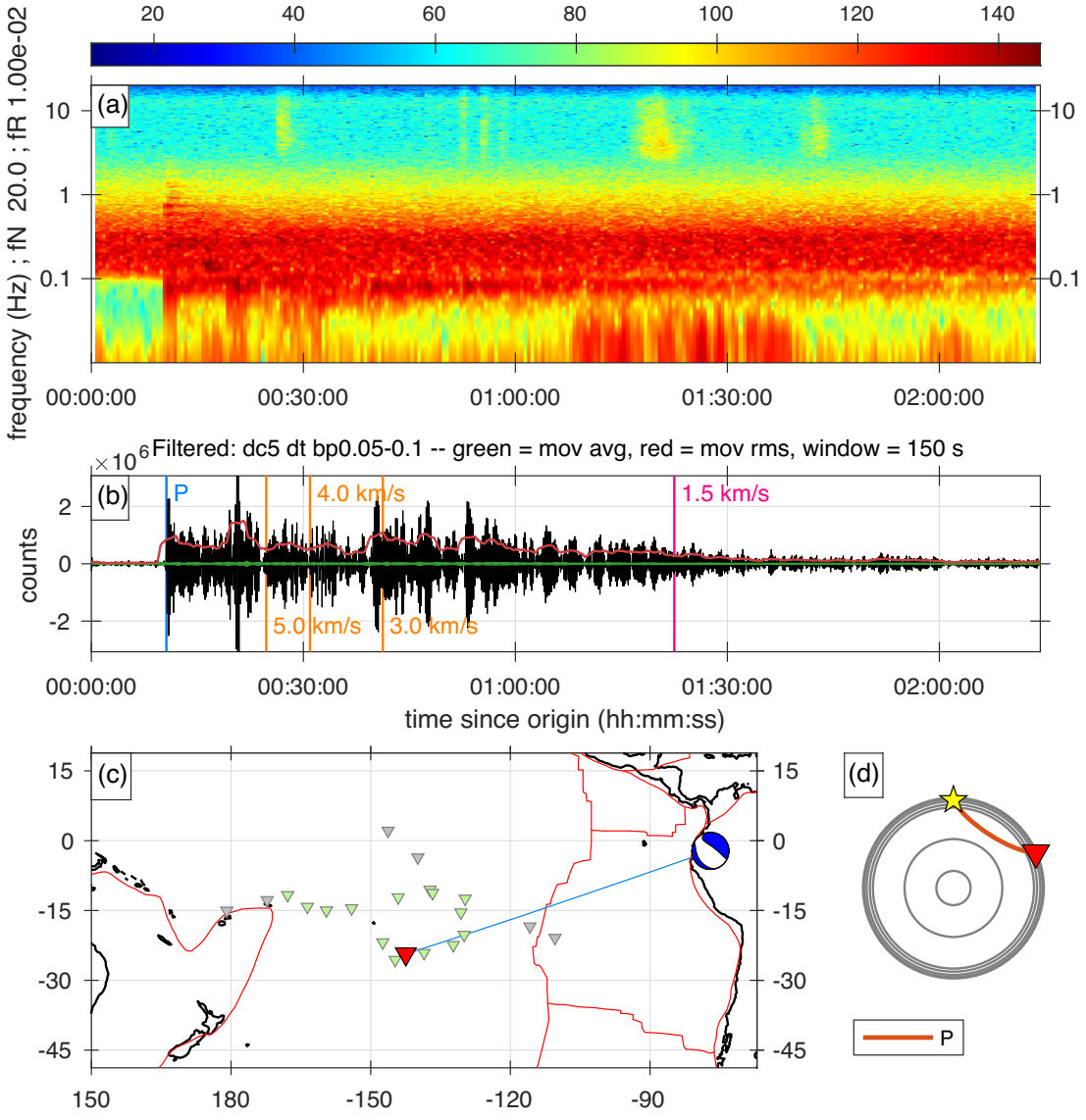

Figure 3. An earthquake that was automatically reported by MERMAID P0023, the magnitude 7.5 Peru-Ecuador border earthquake on 22 February 2019 at 10:17:22.410 UTC. (a) Spectrogram and (b) filtered 0.05–0.10 Hz seismogram. (c) Focal mechanism, ray path to MERMAID P0023 (red triangle) and array configuration at the time of recording (triangles). The green triangles identify other MERMAIDs that also automatically reported the earthquake arrival. (d) Cross section through Earth showing the path of the *P* wave from the event (yellow star, rotated to the North Pole) to MERMAID P0023 (red triangle).

and *S* conversions) and hydroacoustic *T* phase arrivals. An example for an interval that contains a teleseismic earthquake is shown in Fig. 2. The spectrogram is shown in Fig. 2(a), the spectral density compared to the background for the month in Fig. 2(b). Raw pressure time-series are shown in Fig. 2(c). Data filtered between 2 and 10 Hz appear in Fig. 2(d), and in the band 0.05–0.10 Hz in Fig. 2(e). Filtering is accomplished using two-pass, two-pole Butterworth filters. For the lowest-frequency bandpass, the time-series was decimated by a factor of 5 prior to filtering. Moving averages (in green) and moving averages of rms values (in red) over 30 s intervals are plotted overlaying the traces in Figs 2(c)–(e).

Spectrograms were computed using moving segments of 100 s length and with 70 per cent overlap, windowed using a single prolate-spheroidal taper with a concentration of four times the fundamental frequency (Simons *et al.* 2009). Spectral densities were computed using the Chave *et al.* (1987) algorithm on hour-long segments using the same windowed segmentation, with bootstrap error estimates. When reporting spectral densities over longer time periods, we show the median, 5th and 95th percentiles of their distribution over the time interval of interest. Fig. 2(b) is an example of both modes of presentation, where the spectrum of the hour-long data segment shown in Fig. 2(c) is shown (in red) against the background spectrum for the month during which it was acquired (in blue), so that the transient increase in spectral power evident from Fig. 2(a) can be appreciated against the context of the background ambient noise.

3 SIGNAL: EARTHQUAKES AND OTHER TRANSIENTS

In this section we designate as 'signal' all short-time transients of any origin that stand out from a continuous, longer-time, background after manual analysis and visual inspection.

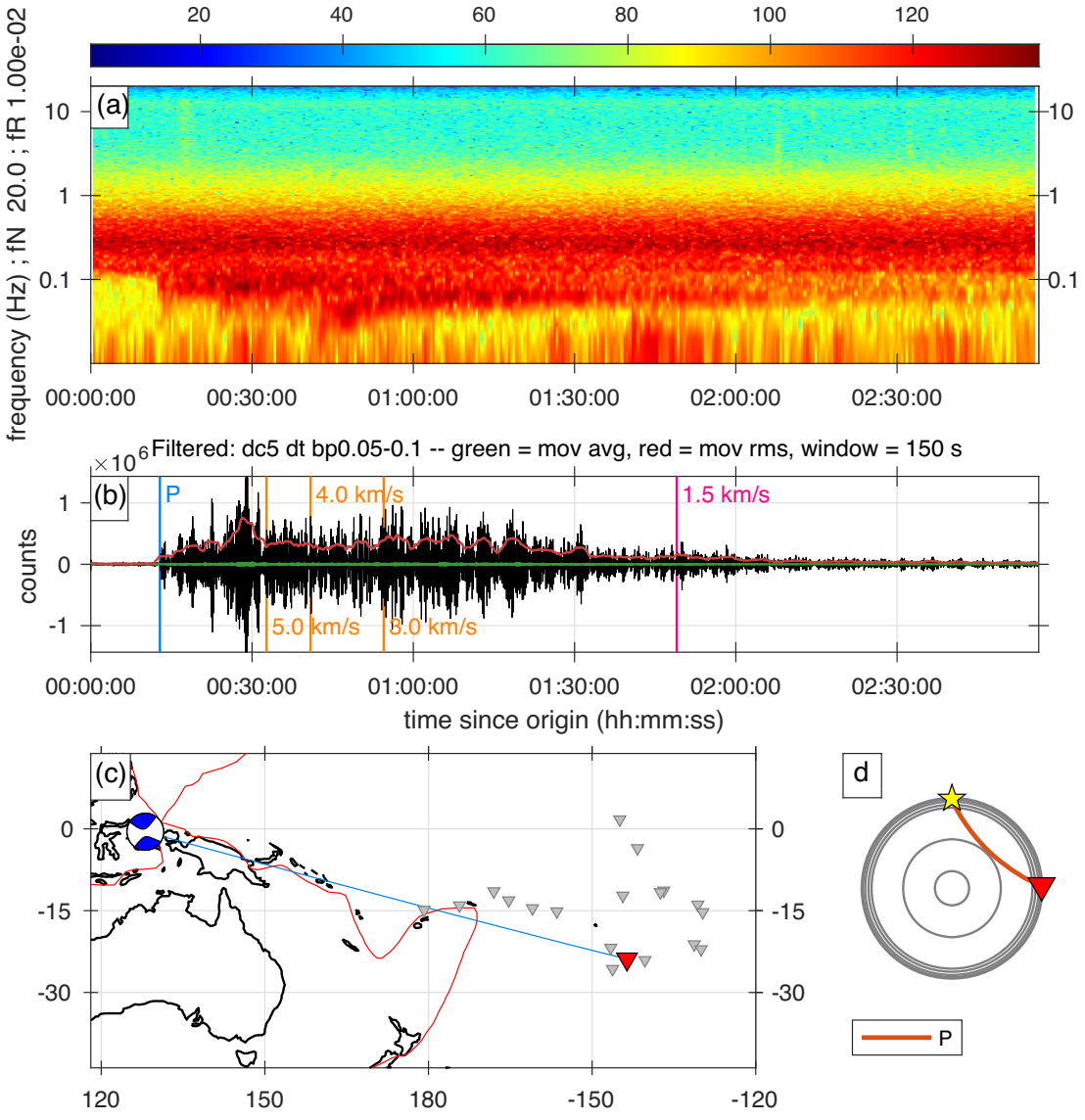

Figure 4. An example of an event that was not automatically reported by MERMAID P0023, the magnitude 7.3 Halmahera, Indonesia earthquake on 14 July 2019 at 09:10:50.533 UTC. Figure layout, labels and annotations as in Fig. 3. Note the difference in structural complexity of the travel path, along the active subduction zone, compared to the path for the event in Fig. 3.

3.1 Earthquakes of known and unknown origin

MERMAID P0023 automatically reported ten 200–250 s long acoustic data segments that could identifiably be matched to global earthquakes following the procedure of Simon *et al*. (2021a). For 8 of these, the triggering caused the recording to be halted and the ascent to be initiated, resulting in truncated records. However, some triggered segments were kept in memory without interrupting data acquisition, earmarked for later, lower-priority reporting. The complete signatures of those events remained in the record that was ultimately recovered.

Fig. 2 is an example of such a case, displaying the magnitude 6.7 earthquake (IRIS ID 10997608) that occurred at a depth of 55 km on 20 January 2019 at 01:32:52.480 UTC near the coast of Coquimbo, Chile, when MERMAID floated at an epicentral distance of 62.17°. In the `ak135` reference model (Kennett *et al*. 1995), the *P* and *S* waves from this earthquake arrive at 615.52 and 1116.87 s, respectively. Their seabed conversions to acoustic pressure in the water column are visible in the spectrogram (Fig. 2a), as brief increases of power in the range 0.08–0.10 Hz. The third instance of increased energy occurs between 0.03 and 0.10 Hz around 30 min after the origin time, for an equivalent speed of 3.84 km s^{-1} along the Earth's surface. The power spectral density for the same time interval (Fig. 2b) shows the deviation of energy in the band 0.05–0.1 Hz for this hour-long segment compared to the expectation for the entire month of January. The raw time-series is shown in Fig. 2(c), with the 30 s moving average overlaid in green, and the equivalent moving rms value superimposed in red. The 2–10 Hz filtered time-series (Fig. 2d) shows the *P* arrival at 10 min, as well as a brief spike around 30 min. In the 0.05–0.10 Hz filtered seismogram (Fig. 2e) we clearly see that the arrival emerging around the 30-min mark represents the surface wave train, while the *P* arrival remains visible as well.

All 10 of the automatically reported events showed similar spectral energy fingerprints, and good time-domain signal-to-noise

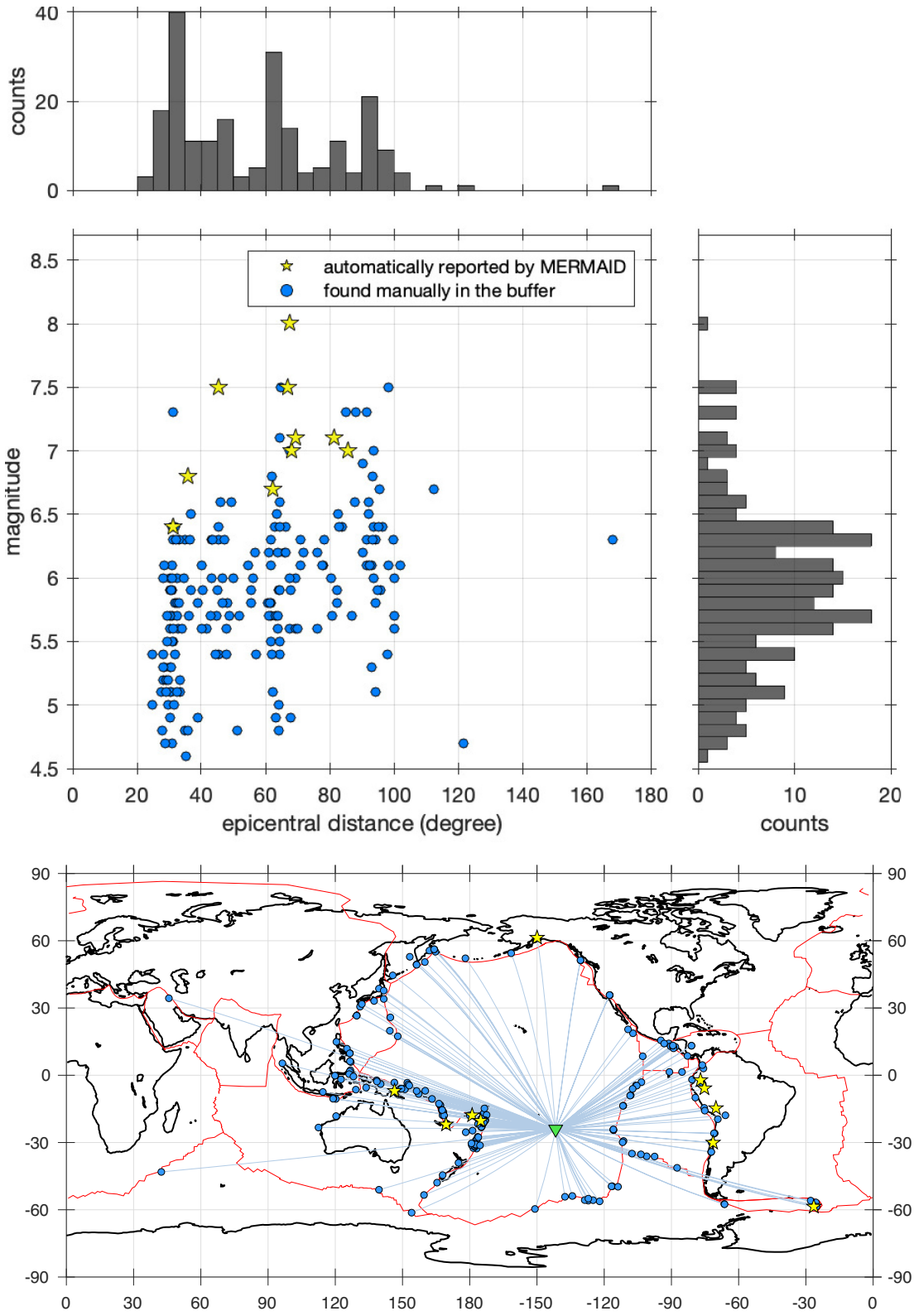

Figure 5. Distributions of epicentral distances and magnitudes of the 213 earthquakes identified in the buffer, out of 274 candidates. The yellow stars are those earthquakes that had been automatically reported by MERMAID, all the others were found by our visual analysis of the memory buffer. The 213 identified earthquakes match events known to the USGS NEIC PDE global catalogue.

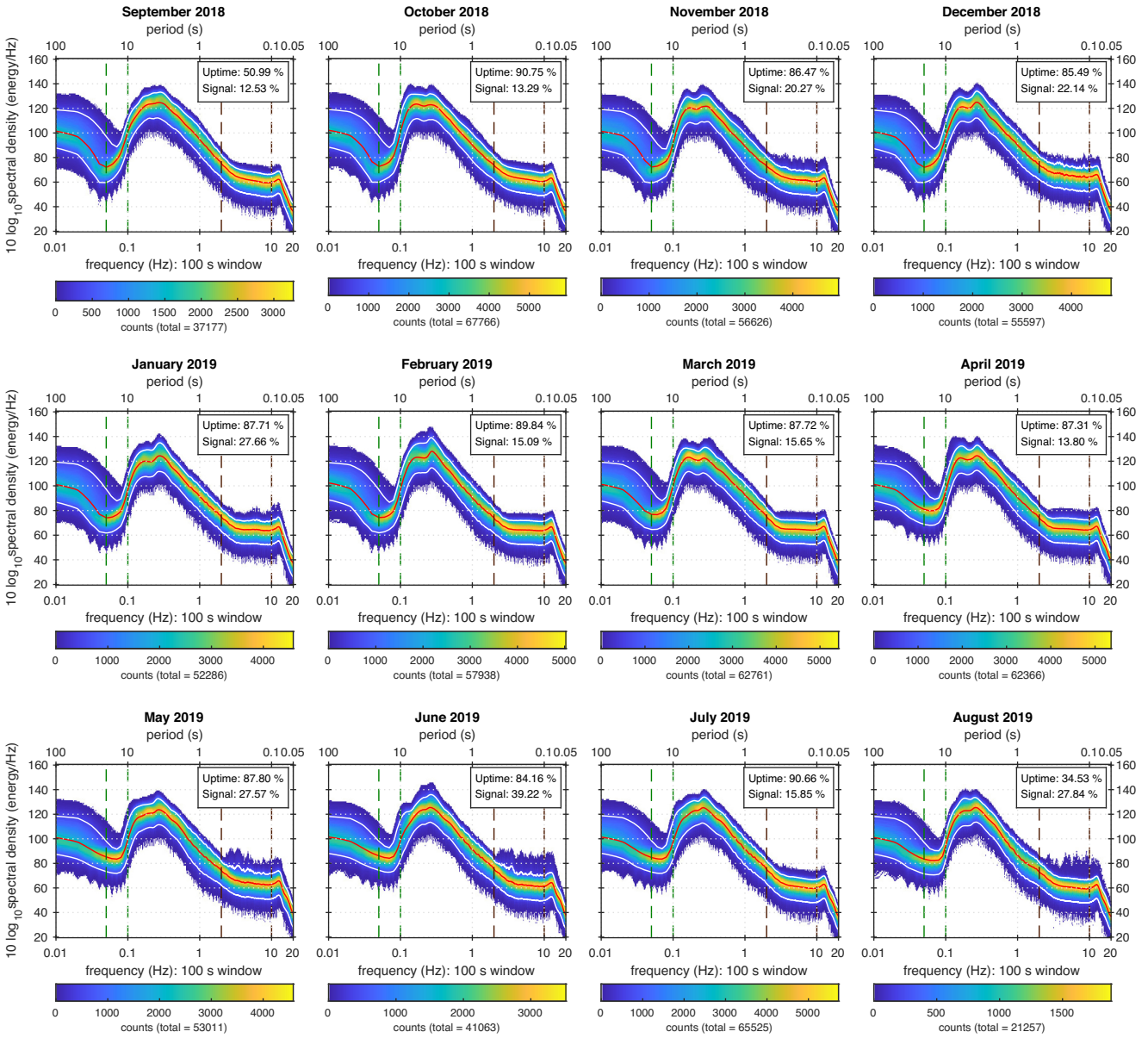

Figure 6. Monthly summaries of low-frequency noise recorded by MERMAID P0023. Each panel represents a population of spectral densities determined from segments analysed with 100 s overlapping windows as explained in the text. The colours correspond to the population density of noise curves, with their total numbers listed in the colour bar below. The red curve is the median, and the white curves the 5th and 95th percentiles. 'Uptime' refers to the percentage of time within the month for which MERMAID's recording of acoustic pressure was available. 'Signal' refers to the percentage of the record that contained signal that we removed prior to spectral density computation. The seismoacoustic frequency range in which earthquakes are clearly seen, 0.05–0.10 Hz, is marked by green dashed vertical lines. The hydroacoustic frequency range where *T* phase arrivals are observed, 2–10 Hz, is marked by brown dashed vertical lines.

ratios in the 0.05–0.10 Hz range for the *P* and/or surface wave arrivals. Hence we took these signatures as the basis to hunt, by visual inspection, for earthquake activity throughout the data set. In this manner we found no fewer than 274 segments containing likely earthquake arrivals.

Approximate MERMAID locations at the corresponding times were obtained by linearly interpolating between surfacing locations. Subsequently we queried (using `irisFetch.m`) the USGS NEIC PDE catalogue maintained by IRIS for global earthquakes and computed (using `taupTime.m`) traveltimes within the `ak135` velocity model. We retained events whose body-wave arrivals fell within three minutes from the times that we had identified in our time-series. When the segment contained a likely surface wave, we chose the catalogue earthquake whose surface wave arrival would imply a speed between 3 and 5 km s^{-1}.

Following this procedure resulted in 213 out of the 274 candidates being positively associated with a catalogue earthquake. Fig. 3 shows another previously reported earthquake, and Fig. 4 one that had not already been reported by MERMAID, for comparison.

Fig. 3 shows the pressure-converted wave train from a magnitude 7.5 earthquake (IRIS ID 11007849) that occurred at a depth of 132 km in the Peru-Ecuador border region on 22 February 2019 at 10:17:22.410 UTC, at an epicentral distance of 66.77°. The arrival did not trigger ascent yet was reported by MERMAID P0023 (and by 14 others in our fleet of 16 instruments). The amplitudes of the *P* and *S* body waves far exceed the background noise, and they are

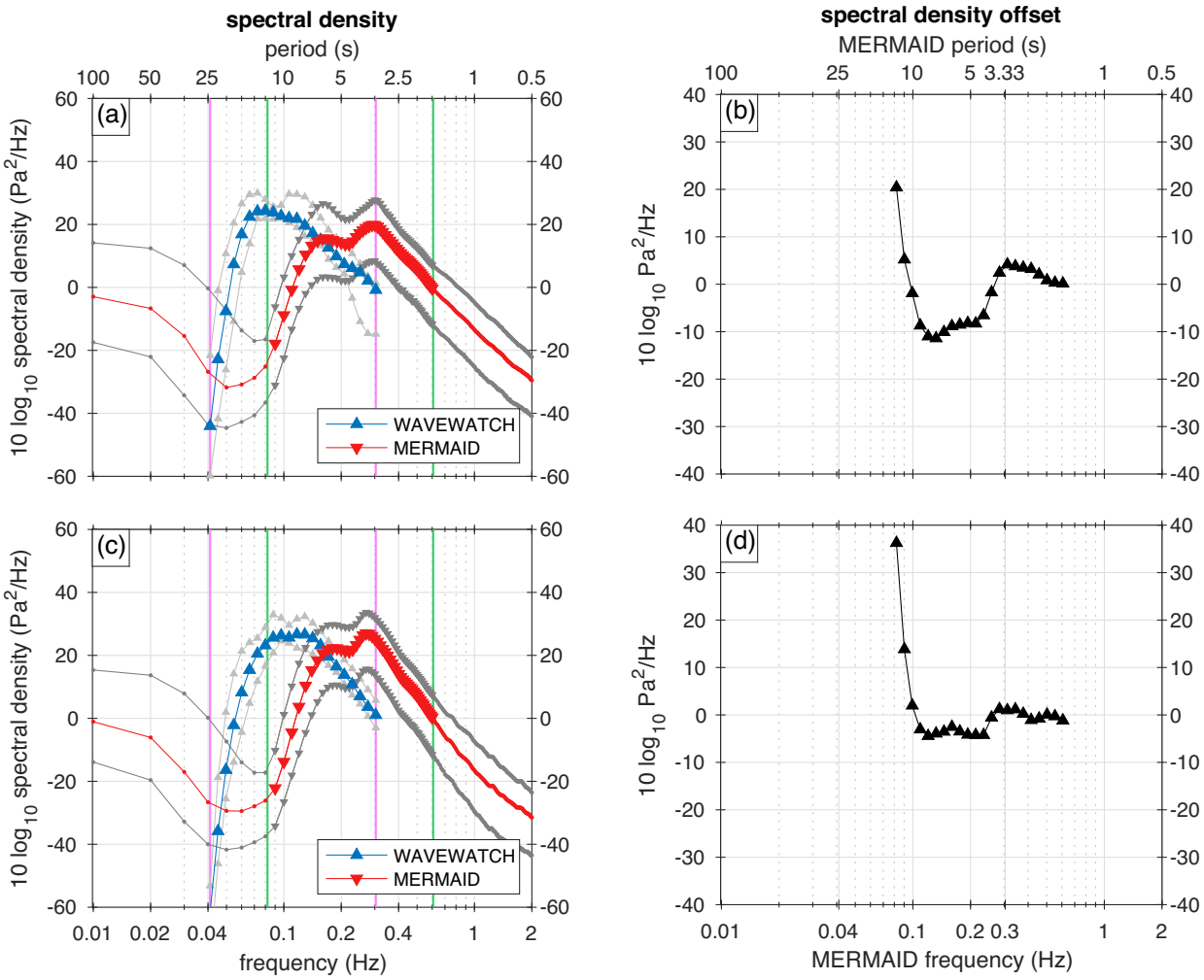

Figure 7. Spectral density of ocean acoustic noise recorded by MERMAID P0023 compared to that of sea-surface pressure from the WAVEWATCH III Hindcast Model, for two different weeks. (a, c) Spectral density of the WAVEWATCH III surface pressure model (blue triangles), and the spectral density of the acoustic pressure noise data recorded by MERMAID (filled red circles and triangles). Solid vertical lines mark the boundaries of the compared frequency ranges: pink for WAVEWATCH III and green for MERMAID. (b, d) Vertical offset between the (interpolated) log-spectral densities of WAVEWATCH III and MERMAID pressure, quoted at the recorded MERMAID frequencies, which are double those of the WAVEWATCH III driving frequencies. Panels (a) and (b) are for the week of 8–15 November 2018, (c) and (d) are for the week of 21–28 February 2019.

clearly visible in the spectrogram, Fig. 3(a), and in the time-domain record, Fig. 3(b). Focusing on the 0.05–0.1 Hz frequency band, surface waves are seen to follow, and in the time-domain we marked the times associated with speeds along the surface of 5, 4 and 3 km s^{-1}. In the higher frequency ranges, between 2 and 10 Hz, hydroacoustic arrivals are observed in the spectrogram. Since the propagation path of any *T* waves generated by this earthquake is almost entirely in the water, we marked the 1.5 km s^{-1} arrival on the record as well. Fig. 3(c) shows a map with the location of the earthquake and the array configuration at the time of its recording, and Fig. 3(d) shows the `ak135` ray path on a cross-section through Earth.

Fig. 4 shows the magnitude 7.3 Halmahera, Indonesia, earthquake (IRIS ID 11073718) that occurred at a depth of 10 km on 14 July 2019 at 09:10:50.533 UTC, at an epicentral distance of 88.24°. Smaller than the event shown in Fig. 3 and almost 22° more distant, this particular event did not trigger automatic reporting by MERMAID P0023 nor by any other MERMAID instrument. The *S* and surface wave arrivals are not as clearly differentiated as in Fig. 3, and any *T* wave arrivals are not obvious.

The Supporting Information contains the full complement of waveforms identified in the manner described in this section. Most of these lead with a mantle *P*-wave arrival, though there are some that contain core-transmitted waves. Simon *et al*. 2021b provide a detailed discussion of these and other phases beyond *P* heard by MERMAID.

Fig. 5 summarizes the distributions of epicentral distances and magnitudes of all 213 identified earthquakes. Their magnitudes span the range from 4.6 to 8.0, with the majority between magnitude 5.5 and 6.5. Events that had already been reported by MERMAID (yellow stars) have magnitudes of 6.4–8.0, ranking among the largest of the recorded set. Most identified earthquakes occurred in the Pacific Ocean around the Ring of Fire and the East Pacific Rise. The furthest earthquakes are at 168.10° distance. We found no matches in the catalogue smaller than magnitude 4.4 or closer than 24.78°, the distance to the nearest major plate boundary. On the other hand, our analysis comprises several ($274 - 213 = 61$) arrivals from candidate earthquakes that remain as yet unidentified. Those could arise from closer events not reported to the USGS NEIC PDE database.

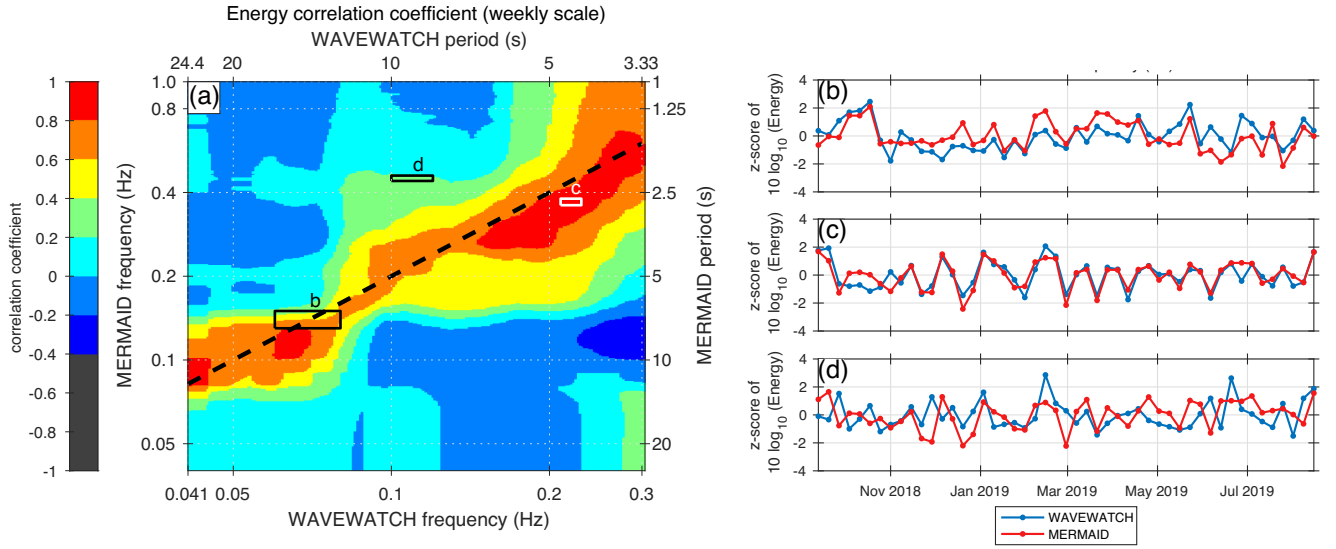

Figure 8. Correlation between ocean acoustic noise recorded by MERMAID P0023 and WAVEWATCH III sea-surface pressure over the year-long observation period. (a) Correlation coefficients in narrow frequency bins. The dashed black line links ocean-wave frequencies on the horizontal axis to acoustic-pressure frequencies on the vertical axis. Boxes marked b, c, and d are called out for analysis in the three panels to the right. (b) Energy time-series in a portion of the band that lies on the frequency-doubling line. The WAVEWATCH III ocean-wave frequency band is 0.06–0.08 Hz and the MERMAID pressure frequency band 0.13–0.15 Hz. Their correlation coefficient is 0.559. (c) Another example for frequencies lying along the double frequency line, 0.21–0.23 Hz for WAVEWATCH III and 0.36–0.38 Hz for MERMAID. Their correlation coefficient is 0.845. (d) An example of the correlation coefficient off the frequency-doubling line, WAVEWATCH III in the 0.10–0.12 Hz band and MERMAID between 0.44 and 0.46 Hz. Their correlation coefficient is 0.150.

3.2 Other transients: *T* phases, ship traffic, bursts and swarms

We performed a search for transient signals in a manner reminiscent of traditional STA/LTA analysis (Allen 1978) by computing a short-time (30 s) moving-window rms time-series of the 2–10 Hz filtered data, and comparing it to a long-term (3 hr) windowed version. We used an iterative procedure to obtain a stable long-term average.

After computing a 3-hr moving-window average version (denoted *L*3.0) of the 30 s moving-window rms record (denoted *S*30.0), we replace the values of *S*30.0 by those of *L*3.0 whenever the values in *S*30.0 exceeded those in *L*3.0. This results in a new short-term average sequence, *S*30.1. From this we compute a new long-term average *L*3.1, and again we threshold the values in *S*30.1 to those in *L*3.1, and so on. After three iterations, a threshold of 1.5 for the ratio of the original short-time average (*S*30.0) to the final long-term average (*L*3.3) was used to identify intervals of transient power excess, many of which lasted for about 5–10 min each.

As expected, this transient detection method captured multiple isolated *T* phases, phases with emergent onsets, a well-defined duration on the order of minutes, and occupying a wide frequency band. See, for example, Fig. A1. For immediate comparison with an acoustic earthquake conversion we show Fig. A2, which displays a sharper onset and a much lower-frequency occupied bandwidth.

In addition, we identified a number of intervals with noise due to ships, characterized in the time-frequency domain by energy dominating a narrow frequency band over periods of time that are usually longer than a few minutes but not more than a few hours (Simons *et al*. 2009). The power spectral density of ship noise contains peaks with narrow widths, for example at 6, 8, 10, 12, 14 and 16 Hz. See, for example, Fig. A3.

Finally, the record contains a large number of repeated bursts of energy spanning the range 2–20 Hz, each of them lasting a handful of minutes and separated from each other by 2–5 min. Periods with such anomalous activity often lasted several days, beginning slowly, growing over time to reach a peak from which they gradually subsided at about the same rate. Storms could be thought to be responsible for these episodes (Gualtieri *et al*. 2018). However, we made detections, for example between June 2019 and August 2019, that did not correspond to any known cyclone occurrence in the Southern Pacific in the International Best Track Archive for Climate Stewardship (IBTrACS) database. Swarms of nearby small earthquakes, or *T* phases, could be another possible explanation (e.g. Talandier & Okal 2001; Talandier *et al*. 2016; Simon *et al*. 2021b), but we were unable to identify any precursory body wave or surface wave arrivals. Finally, submarine volcanic activity may be responsible (e.g. Metz *et al*. 2016). Further investigation is needed into the nature of these transient episodes, but for now, we removed them from the record. Two examples are in Figs A4 and A5. The spectrogram of Fig. A4 is rendered linearly in the frequencies between 0–20 Hz, while that of Fig. A5 has a logarithmic frequency axis limited to 0.01–20 Hz.

An example record with no detectable transients at all is shown in Fig. A6 and another one with very little activity in Fig. A7, again using a logarithmic and a linear spectrogram frequency scale, respectively. Fig. A7 contains the hour of quiescence before the arrival of the seismoacoustic earthquake conversions shown in Fig. A8, where we note that Fig. A8 is a version of Fig. 2 that omits the noise spectral density for the entire month. Fig. A9 shows the signature earthquake of Fig. 2 in a layout easily compared with Figs 3 and 4.

4 INFRASONIC AMBIENT NOISE AND ITS SEASONALITY

The removal of clearly detected or merely suspected earthquakes, seismoacoustic and hydroacoustic phases, and other transients from the yearly record amounted to the cutting of 1459 hr of ‘signal’, leaving 5570 hr of ‘noise’, whose time-evolving spectral density we now discuss.

Fig. 6 is the monthly summary of this infrasonic ambient noise. It peaks between 0.01–0.03 and 0.10–0.50 Hz, with a much quieter band in-between. Noise levels come down as the frequency rises above 0.50 Hz. The significant drop above 14 Hz is due to filtering of the data in post-processing, and we also note that the instrument begins to lose sensitivity at the low frequencies below about 0.1 Hz. While it is hard to make out details on a logarithmic scale without closer scrutiny, it is readily apparent that the noise spectral densities vary from month to month. For example, at 0.05 Hz the spectral density fell below 80 on our logarithmic scale during September 2018–March 2019, but rose above 80 during April–August 2019. In order to quantitatively describe the variation of the background noise, we studied the temporal variations of energy levels integrated over distinct frequency bands of interest, primarily between 0.05–0.10, 0.10–0.50 and 2–10 Hz, where we found the most significant temporal variation.

To attribute the observed time-dependence to a particular physical mechanism, we investigated the influence of the weather on the ambient noise field in the ocean. Wind and swell are the cause of ocean surface gravity waves, and when two ocean wave trains arrive from opposite directions, they generate a pressure field at double the driving frequency that attenuates only weakly with depth (Longuet-Higgins 1950; Hasselmann 1963), registering on ocean bottom seismometers (Babcock *et al*. 1994; Webb 1998) and rather prominently as Rayleigh and Love (Gualtieri *et al*. 2020, 2021) surface waves on seismometers on land (Gualtieri *et al*. 2013, 2014; Nakata *et al*. 2019). We correlate the time-evolving spectral density of our MERMAID noise record with the spectral density of the equivalent surface pressure from the WAVEWATCH III Hindcast Model (WAVEWATCH III Development Group 2019). The model used wind speed to derive surface pressure and its spectral density between 0.041 and 0.304 Hz in 3-hr intervals. We computed the medians of these spectral density models of the driving process at the matching geographic location over week-long windows, for comparison with the spectral density received by MERMAID at depth of 1500 m.

Fig. 7 shows two examples, for the weeks of 8–15 November 2018 and 21–28 February 2019. In this figure, we deconvolved the MERMAID transfer function from the record (see also Burky *et al*. 2021), so the units of the WAVEWATCH III and the MERMAID spectral densities match (both are $Pa^2\ Hz^{-1}$). Figs 7(a) and (c) clearly show their matching shapes, and the relative flatness of the offset is apparent from Figs 7(b) and (d). The MERMAID spectral density is shown by the red triangles, with a dark grey envelope containing the 5th and 95th percentile of the values over the week, respectively. The WAVEWATCH III spectral density is shown in blue triangles, within a 5th and 95th percentile band of light grey triangles.

We computed the temporal evolution of the energy comprised within logarithmically evenly spaced frequency intervals, both for the surface pressure of the WAVEWATCH III Hindcast Model and for the noise recorded by MERMAID, over the entire year-long period. Each data point in the time-series is obtained from the spectral density computed over a week-long window. The resulting map of the correlation coefficients between both time-series is shown in Fig. 8(a). They are highest along the double-frequency line (examples labeled in Figs 8b and 8c), validating the assertion that surface-driven processes drive the infrasonic ambient noise in the 0.08–0.6 Hz range. Fig. 8d shows a counterexample. The WAVEWATCH III model does not provide any information at higher frequencies, hence MERMAID's records in this range have the potential to become primary environmental data.

5 CONCLUSIONS

Over the course of an 11-month period, a freely drifting hydroacoustic MERMAID float automatically reported short seismograms from two handfuls of triggered teleseismic earthquakes. An exceptional recovery allowed us to analyse the full, nearly continuous, record preserved on board. Our analysis reveals that MERMAID P0023 recorded no fewer than 213 teleseismic events of magnitude above 4.5, various transients and an interpretable record of background noise. The earthquakes detected corresponded to 2.38 per cent of events present in the global seismic catalogue between 13 September 2018 and 15 August 2019. A detailed discussion of what MERMAID's return rates (under automatic reporting) mean for global seismology, and for seismic tomography in particular, is provided by Simon *et al*. (2021a), and interpreted examples of non-primary arrivals (often included with the automatically reported segments) are given by Simon *et al*. (2021b). In this paper, we largely focused on the novelty of the complete noise record of a MERMAID float that was, rather uncharacteristically, recovered (and returned to active duty). The comparison of the noise series to an independent model of wave height variations shows that infrasonic ambient noise in the 0.08–0.8 Hz frequency band is driven by the interaction between the atmosphere and the ocean at the surface through the well-known frequency-doubling secondary-microseism generating mechanism. A new model MERMAID instrument, which will de-emphasize teleseismic earthquake detection and instead report time-varying noise spectral densities directly, has been designed and constructed. Its deployment is planned within the year, and the results will be reported elsewhere.

ACKNOWLEDGEMENTS

This work was sponsored by the Royal Thai Government, by Princeton University, and by the National Science Foundation under grant OCE-1917058 to FJS and Jessica C.E. Irving. Trajectory data for MERMAID P0023 can be downloaded from `http://www.earthscopeoceans.org`. We thank Joel Simon for help and advice, and Yann Hello and Lucas Sawade for recovering and redeploying the MERMAID float from the R/V *Atalante*, operated by Ifremer and Genavir. We are grateful for the expert handling of the manuscript by Associate Editor, Dr Gabi Laske, and appreciate the thoughtful and helpful reviews by Dr DelWayne Bohnenstiehl and another, anonymous, reviewer.

6 DATA AVAILABILITY AND RESOURCES

Earthquake source locations, times, and magnitudes were obtained from the Incorporated Research Institutions for Seismology (IRIS) and the Federation of Digital Seismograph Networks (FDSN). Focal mechanisms were provided by the Global Centroid Moment Tensor (CMT) project and drawn using `focalmech.m` written by James A. Conder. The software for data analysis was written in MATLAB, and is publicly available from `https://github.com/sirpipat/mermaid_buffer`.

Spectral densities of the surface pressure from the WAVEWATCH III Hindcast Model are from the National Oceanic and Atmospheric Administration (NOAA) Environmental Modeling Center (EMC), accessed at `ftp.ifremer.fr/ifremer/ww3/`.

REFERENCES

Allen, R.V., 1978. Automatic earthquake recognition and timing from single traces, *Bull. seism. Soc. Am.,* **68**(5), 1521–1532.

Babcock, J.M., Kirkendall, B.A. & Orcutt, J.A., 1994. Relationships between ocean bottom noise and the environment, *Bull. seism. Soc. Am.,* **84**(6), 1991–2007.

Bonnieux, S., Cazau, D., Mosser, S., Blay-Fornarino, M., Hello, Y. & Nolet, G., 2020. MeLa: a programming language for a new multidisciplinary oceanographic float, *Sensors,* **20**(21), 6081, doi:10.3390/s20216081.

Burky, A., Irving, J. C.E. & Simons, F.J., 2021. Instrument response removal and the 2020 M_{Lg} 3.1 Marlboro, New Jersey, earthquake, *Seismol. Res. Lett.,* doi:10.1785/0220210118.

Chave, A.D., Thomson, D.J. & Ander, M.E., 1987. On the robust estimation of power spectra, coherences, and transfer functions, *J. geophys. Res.,* **92**(B1), 633–648.

Fox, C.G., Dziak, R.P., Matsumoto, H. & Schreiner, A.E., 1993. Potential for monitoring low-level seismicity on the Juan-de-Fuca ridge using military hydrophone arrays, *Mar. Tech. Soc. J.,* **27**(4), 22–30.

Gualtieri, L., Stutzmann, E., Capdeville, Y., Ardhuin, F., Schimmel, M., Mangeney, A. & Morelli, A., 2013. Modelling secondary microseismic noise by normal mode summation, *Geophys. J. Int.,* **193**(3), 1732–1745.

Gualtieri, L., Stutzmann, E., Farra, V., Capdeville, Y., Schimmel, M., Ardhuin, F. & Morelli, A., 2014. Modelling the ocean site effect on seismic noise body waves, *Geophys. J. Int.,* **197**(2), 1096–1106.

Gualtieri, L., Camargo, S.J., Pascale, S., Pons, F. M.E. & Ekström, G., 2018. The persistent signature of tropical cyclones in ambient seismic noise, *Earth planet. Sci. Lett.,* **484,** 287–294.

Gualtieri, L., Bachmann, E., Simons, F.J. & Tromp, J., 2020. The origin of secondary microseism Love waves, *Proc. Natl. Acad. Sc.,* **117**(47), 29504–29511.

Gualtieri, L., Bachmann, E., Simons, F.J. & Tromp, J., 2021. Generation of secondary microseism Love waves: effects of bathymetry, 3-D structure, and source seasonality, *Geophys. J. Int.,* **226**(1), 192–219.

Hasselmann, K., 1963. A statistical analysis of the generation of microseisms, *Rev.Geophys.,* **1**(2), 177–210.

Hello, Y. & Nolet, G., 2020. Floating seismographs (MERMAIDS), in *Encyclopedia of Solid Earth Geophysics, Encyclopedia of Earth Sciences,* ed. Gupta, H.K., pp. 1–6, Springer, doi:10.1007/978–3–030–10475–7_248–1.

Joubert, C., Nolet, G., Sukhovich, A., Ogé, A., Argentino, J.-F. & Hello, Y., 2015. Hydrophone calibration at very low frequencies, *Bull. seism. Soc. Am.,* **105**(3), 1797–1802.

Joubert, C., Nolet, G., Bonnieux, S., Deschamps, A., Dessa, J.-X. & Hello, Y., 2016. *P*-delays from floating seismometers (MERMAID), Part I: data processing, *Seismol. Res. Lett.,* **87**(1), 73–80.

Kennett, B. L.N., Engdahl, E.R. & Buland, R., 1995. Constraints on seismic velocities in the Earth from travel-times, *Geophys. J. Int.,* **122**(1), 108–124.

Kerman, B.R., 1993. *Natural Physical Sources of Underwater Sound: Sea Surface Sound (2),* Springer.

Longuet-Higgins, M.S., 1950. A theory of the origin of microseisms, *Phil. Trans. R. Soc. Lond., A,* **243**(857), 1–35.

Marra, G. *et al.*, 2018. Ultrastable laser interferometry for earthquake detection with terrestrial and submarine cables, *Science,* **361**(6401), 486–490.

Metz, D., Watts, A.B., Grevemeyer, I., Rodgers, M. & Paulatto, M., 2016. Ultra-long-range hydroacoustic observations of submarine volcanic activity at Monowai, Kermadec arc, *Geophys. Res. Lett.,* **43**(4), 1529–1536.

Nakata, N., Gualtieri, L. & Fichtner, A., 2019. *Seismic Ambient Noise,* Cambridge Univ. Press.

Nolet, G. *et al.*, 2019. Imaging the Galápagos mantle plume with an unconventional application of floating seismometers, *Sci.Rep.,* **9,** 1326, doi:10.1038/s41598–018–36835–w.

Ritsema, J. & Lekić, V., 2020. Heterogeneity of seismic wave velocity in Earth's mantle, *Annu. Rev. Earth. planet. Sci.,* **48,** 377–401.

Romanowicz, B., 2008. Using seismic waves to image Earth's structure, *Nature,* **451,** 266–268.

Simon, J.D., Simons, F.J. & Nolet, G., 2020. Multiscale estimation of event arrival times and their uncertainties in hydroacoustic records from autonomous oceanic floats, *Bull. seism. Soc. Am.,* **110**(3), 970–997.

Simon, J.D., Simons, F.J. & Irving, J. C.E., 2021a. Recording earthquakes for tomographic imaging of the mantle beneath the South Pacific by autonomous MERMAID floats, *Geophys. J. Int.,* doi:10.1093/gji/ggab271.

Simon, J.D., Simons, F.J. & Irving, J. C.E., 2021b. *Seismol. Res. Lett.,* doi:10.1785/0220210052.

Simons, F.J., Dando, B. D.E. & Allen, R.M., 2006a. Automatic detection and rapid determination of earthquake magnitude by wavelet multiscale analysis of the primary arrival, *Earth planet. Sci. Lett.,* **250**(1–2), 214–223.

Simons, F.J., Nolet, G., Babcock, J.M., Davis, R.E. & Orcutt, J.A., 2006b. A future for drifting seismic networks, *EOS, Trans. Am. Geophys. Un.,* **87**(31), 305–307.

Simons, F.J., Nolet, G., Georgief, P., Babcock, J.M., Regier, L.A. & Davis, R.E., 2009. On the potential of recording earthquakes for global seismic tomography by low-cost autonomous instruments in the oceans, *J. geophys. Res.,* **114,** B05307, doi:10.1029/2008JB006088.

Simons, F.J., Simon, J.D. & Pipatprathanporn, S., 2021. Twenty-thousand leagues under the sea: Recording earthquakes with autonomous floats, *Acoust. Today,* **17**(2), 42–51.

Stephen, R.A., Spiess, F.N., Collins, J.A., Hildebrand, J.A., Orcutt, J.A., Peal, K.R., Vernon, F.L. & Wooding, F.B., 2003. Ocean Seismic Network Pilot Experiment, *Geochem. Geophys. Geosys.,* **4**(10), 1092, doi:10.1029/2002GC000485.

Sukhovich, A., Irisson, J.-O., Simons, F.J., Ogé, A., Hello, Y.M., Deschamps, A. & Nolet, G., 2011. Automatic discrimination of underwater acoustic signals generated by teleseismic *P*-waves: a probabilistic approach, *Geophys. Res. Lett.,* **38**(18), L18605, doi:10.1029/2011GL048474.

Sukhovich, A., Bonnieux, S., Hello, Y., Irisson, J.-O., Simons, F.J. & Nolet, G., 2015. Seismic monitoring in the oceans by autonomous floats, *Nat. Commun.,* **6**(1), 8027,

Talandier, J. & Okal, E.A., 2001. Identification criteria for sources of *T* waves recorded in French Polynesia, in *Monitoring the Comprehensive Nuclear-Test-Ban Treaty: Hydroacoustics,* Vol. **158,** pp. 567–603, eds deGroot Hedlin, C. & Orcutt, J., Birkhäuser.

Talandier, J., Hyvernaud, O. & Maury, R.C., 2016. Unusual seismic activity in 2011 and 2013 at the submarine volcano Rocard, Society hot spot (French Polynesia), *Geophys. Res. Lett.,* **43**(9), 4247–4254.

Tolman, L.H., 2009. User manual and system documentation of WAVEWATCH III (TM), version 3.14, Tech. Rep. 276, Environmental Modeling Center, Marine Modeling and Analysis Branch.

Tromp, J., 2020. Seismic wavefield imaging of Earth's interior across scales, *Nat. Rev. Earth Env.,* **1,** 40–53.

WAVEWATCH III Development Group, 2019. User manual and system documentation of WAVEWATCH III, version 6.07, Tech. Rep. 333, Environmental Modeling Center, Marine Modeling and Analysis Branch.

Webb, S.C., 1998. Broadband seismology and noise under the ocean, *Rev. Geophys.,* **36**(1), 105–142.

Williams, E.F., Fernández-Ruiz, M.R., Magalhaes, R., Vanthillo, R., Zhan, Z., González-Herráez, M. & Martins, H.F., 2019. Distributed sensing of microseisms and teleseisms with submarine dark fibers, *Nat. Commun.,* **10**(1), 5778, doi:10.1038/s41467–019–13262–7.

SUPPORTING INFORMATION

Supplementary data are available at *GJI* online.

suppl_data

Please note: Oxford University Press is not responsible for the content or functionality of any supporting materials supplied by the authors. Any queries (other than missing material) should be directed to the corresponding author for the paper.

APPENDIX

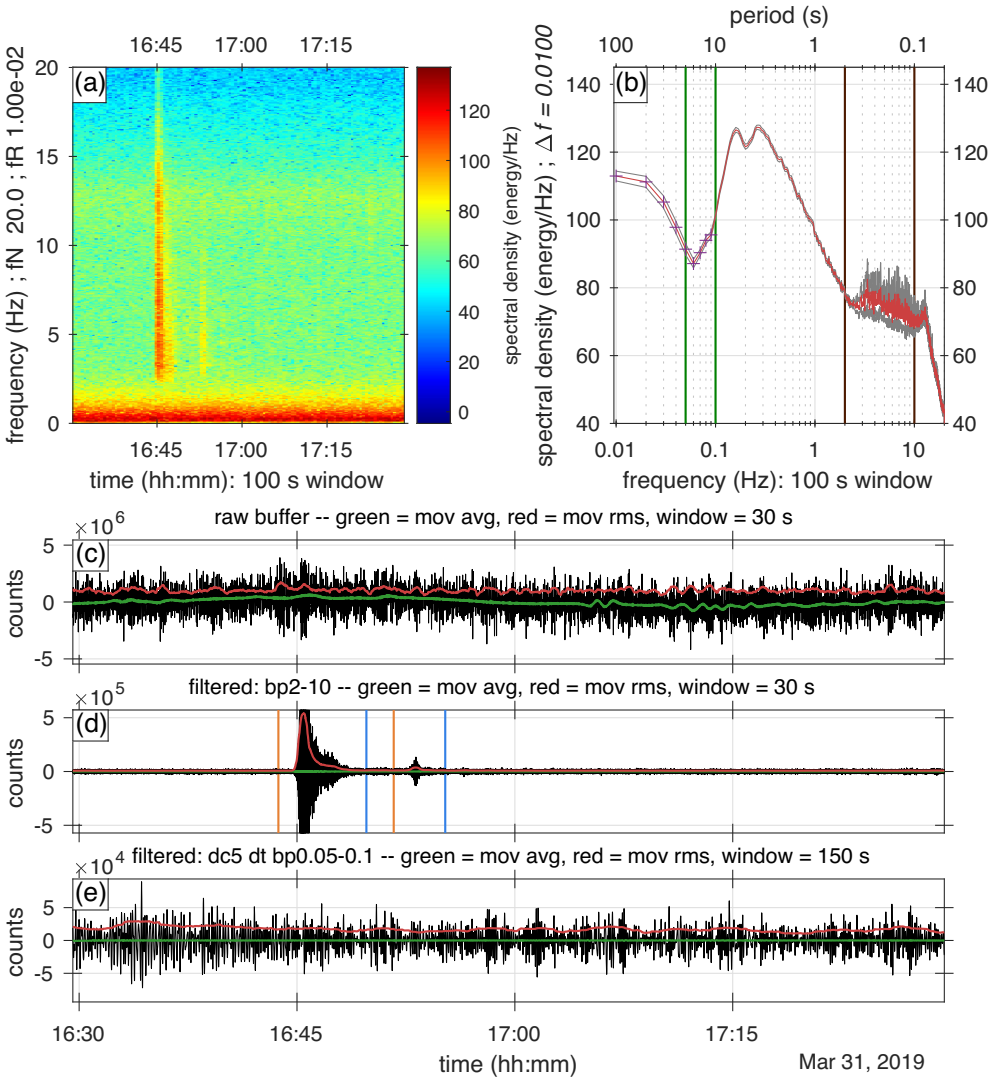

Figure A1. An isolated *T* phase. (a) Spectrogram. (b) spectral density. (c) Raw signal. (d) Filtered signal 2–10 Hz. (e) Filtered signal 0.05–0.1 Hz. The green and red lines in (c)–(e) are moving averages and moving rms values. The orange and blue vertical lines are the beginnings and the ends of the sections removed as discussed in Section 3.2.

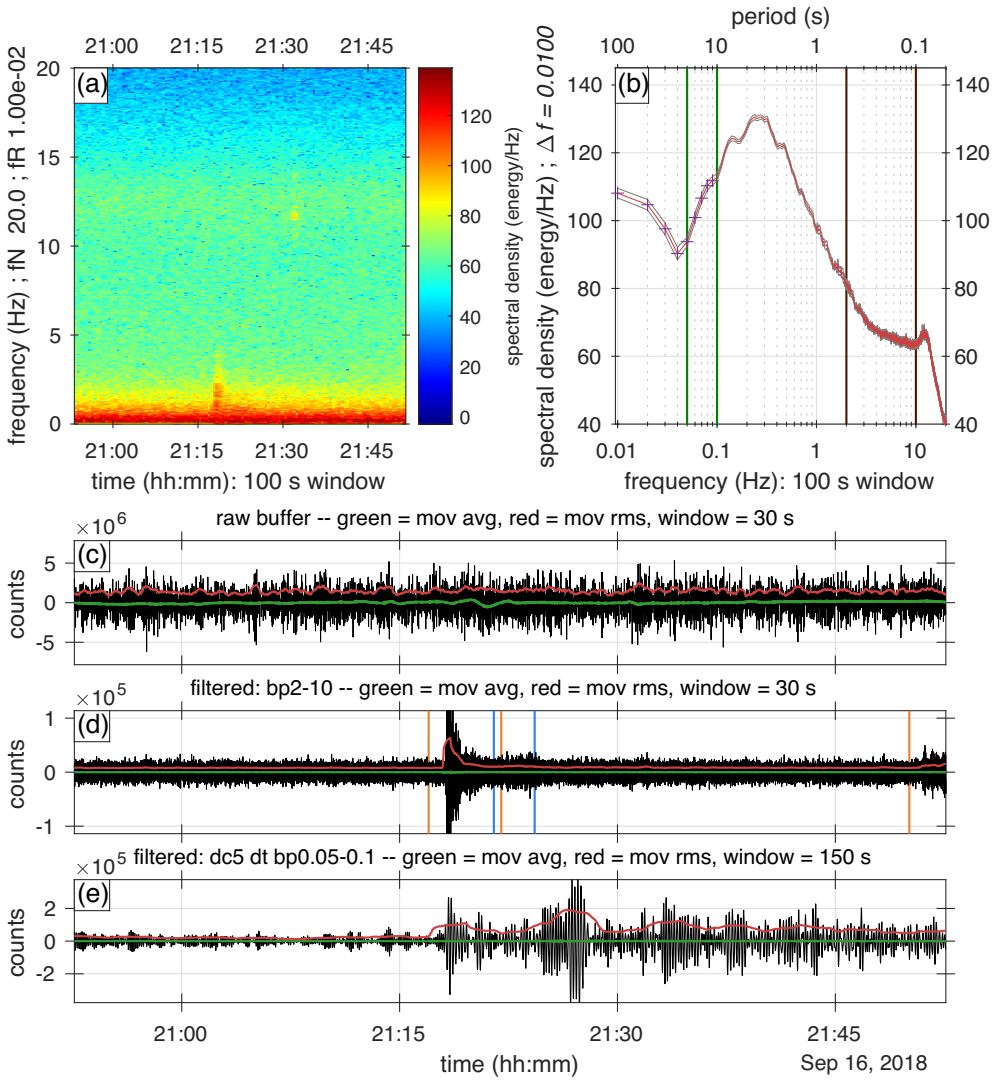

Figure A2. An hour-long section containing an earthquake arrival from the magnitude 6.5 south of Fiji Islands earthquake on 16 September 2018 at 21:11:48.820 UTC. Layout and labelling as in Fig. A1.

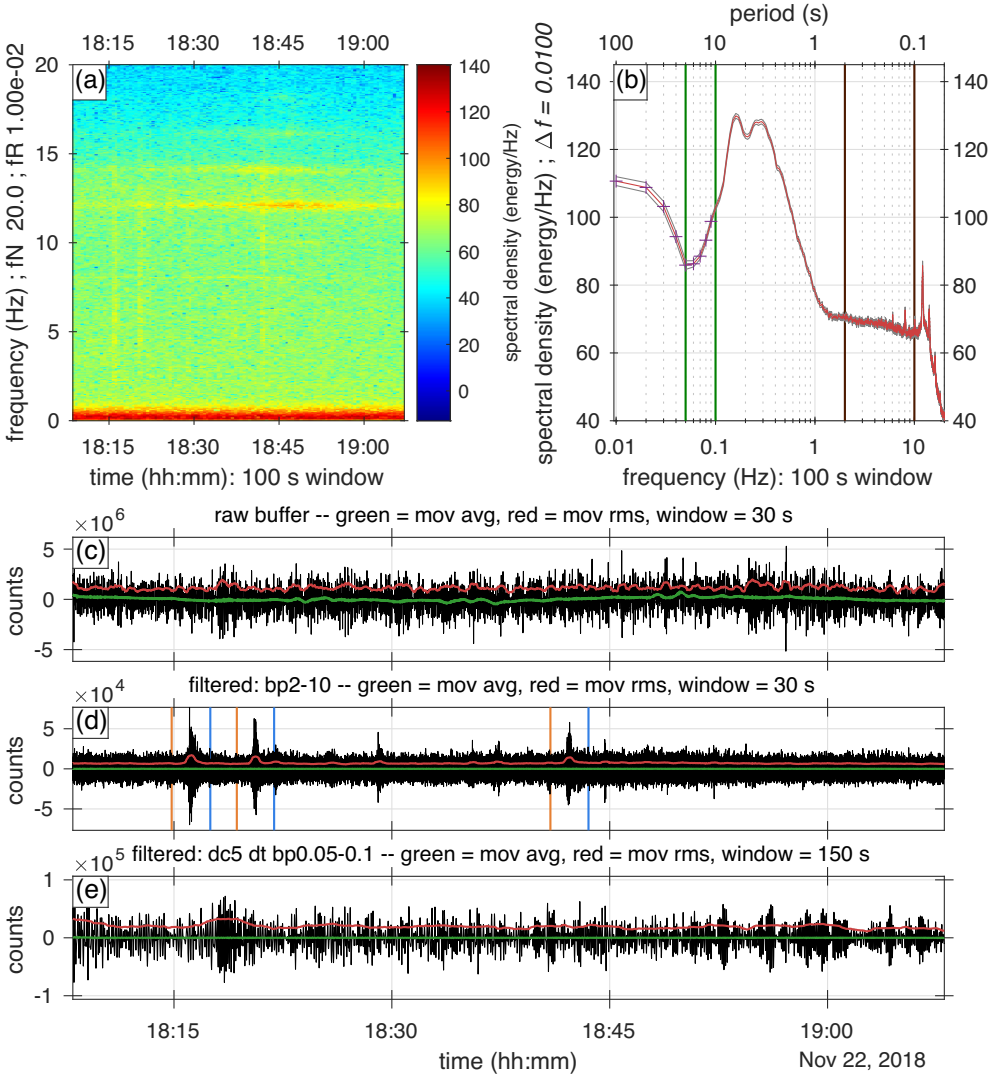

Figure A3. An hour-long section containing ship noise, marked by horizontal stripes in the spectrogram, and narrow harmonic peaks in the spectral density. Layout and labelling as in Fig. A1.

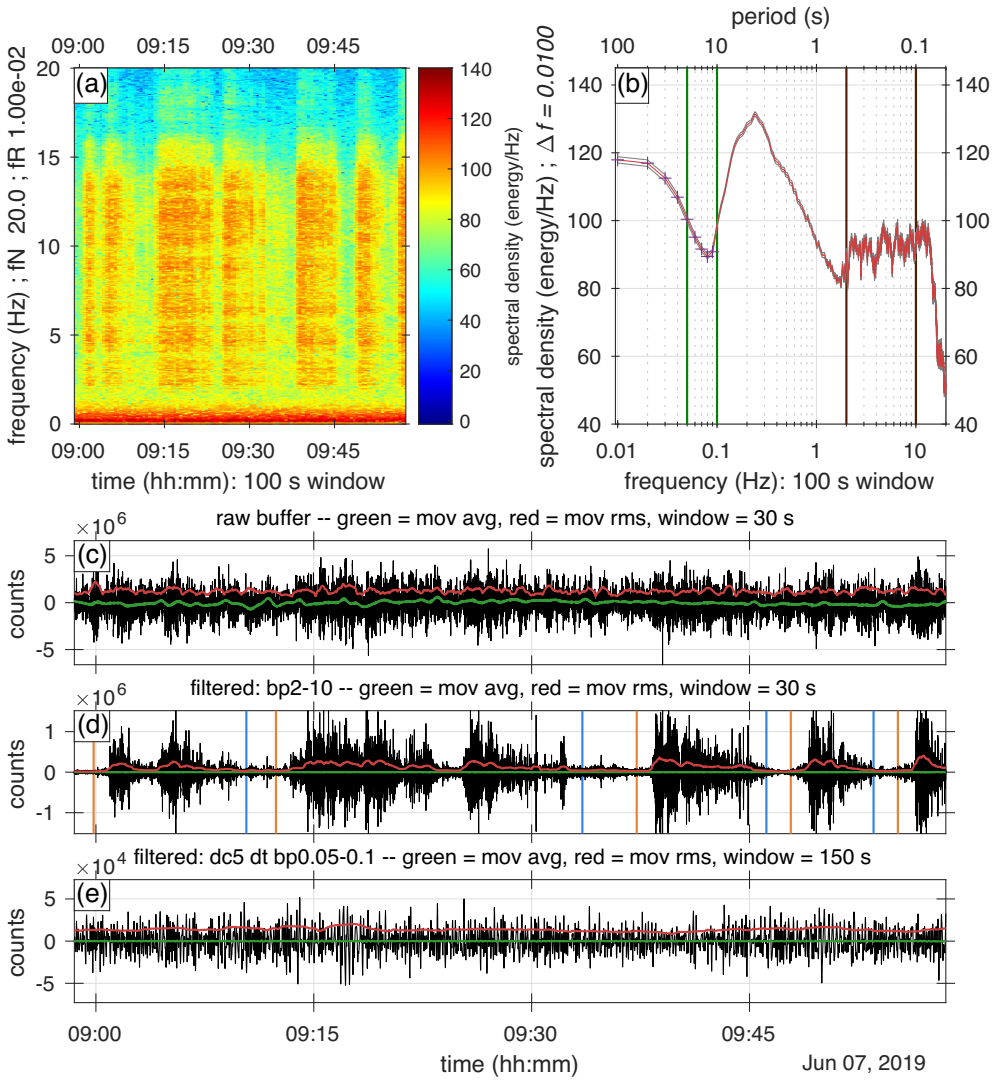

Figure A4. An hour-long section within a swarm period from 6 June 2019, 02:00 UTC to 10 June 2019, 01:30 UTC. Layout and labelling as in Fig. A1.

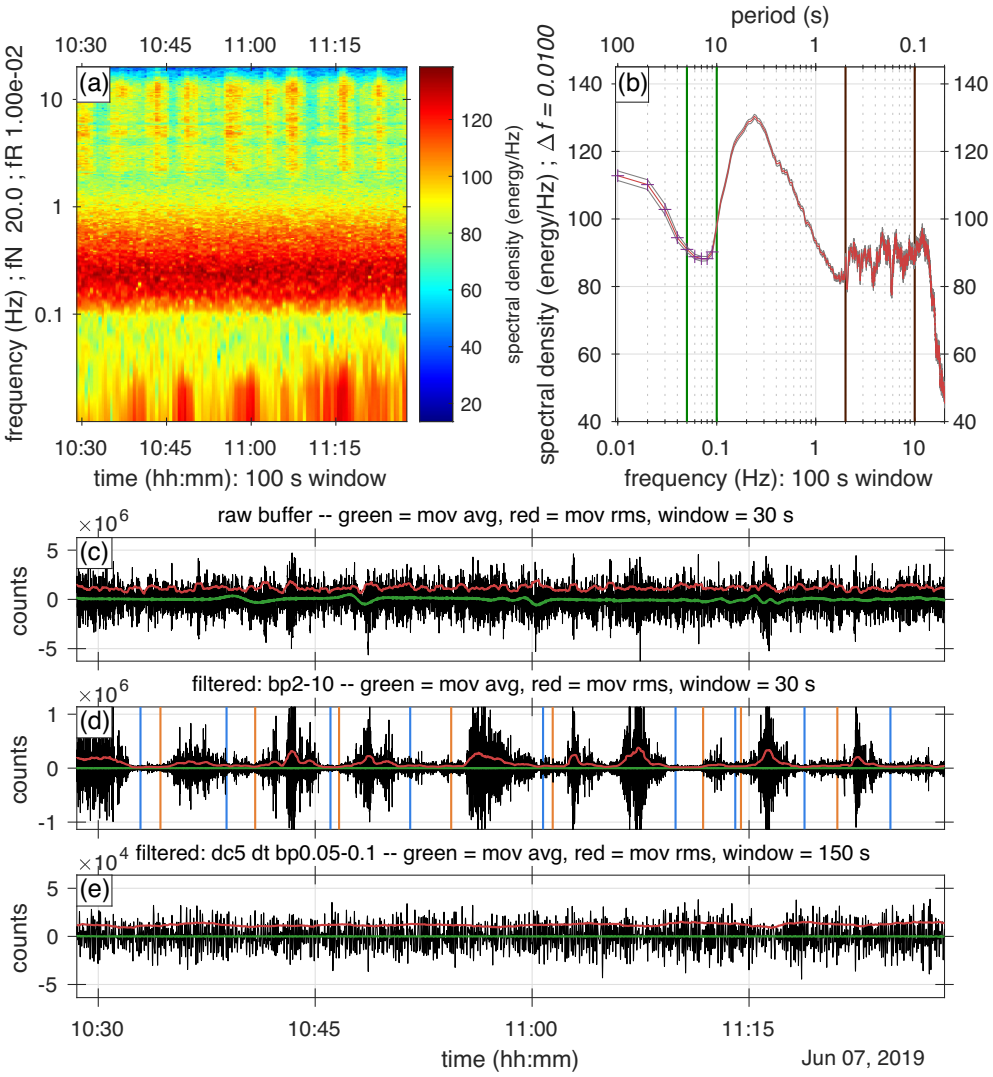

Figure A5. An hour-long section within a swarm period, on a logarithmic frequency axis, for comparison with Fig A4. Layout and labelling as in Fig. A1.

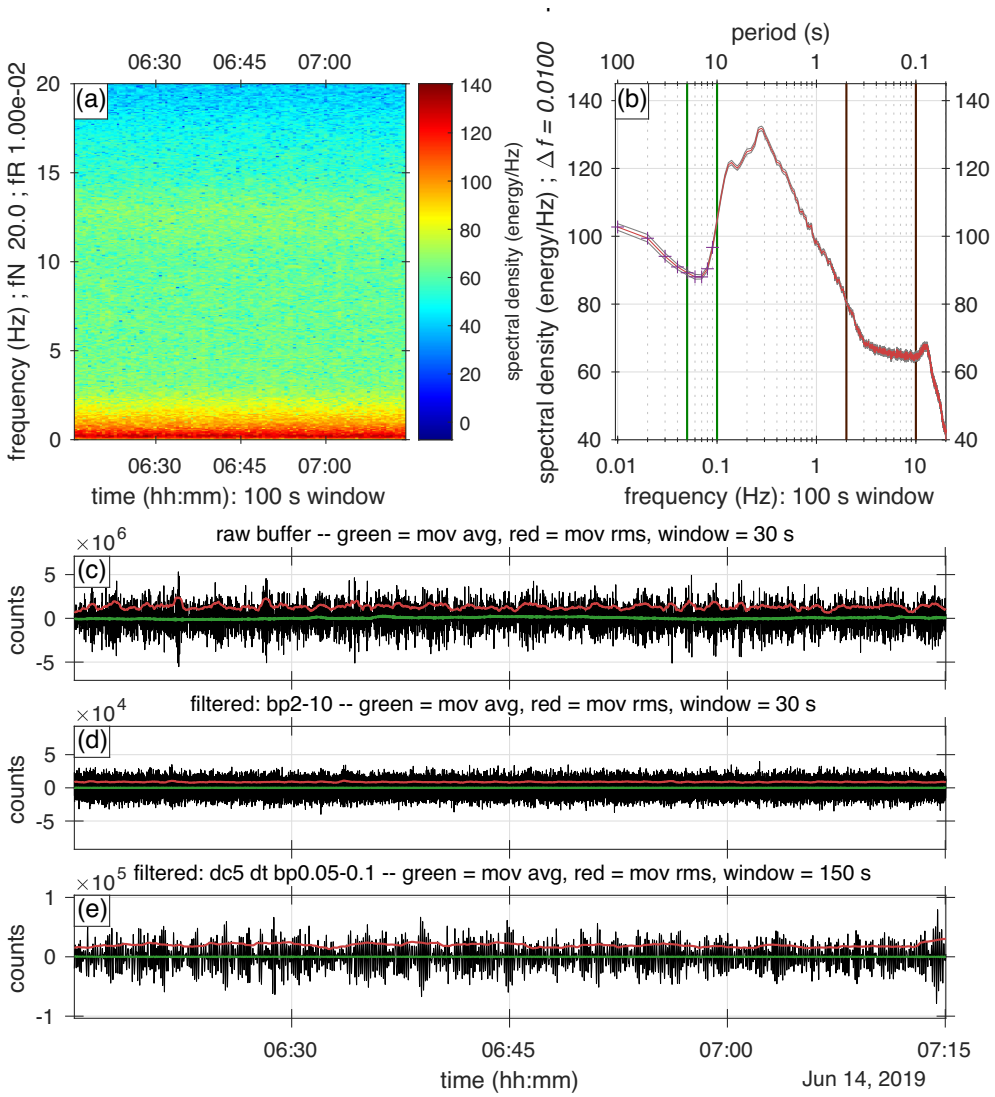

Figure A6. An hour-long section without transients, that is, only infrasonic ambient noise. Layout and labelling as in Fig. A1.

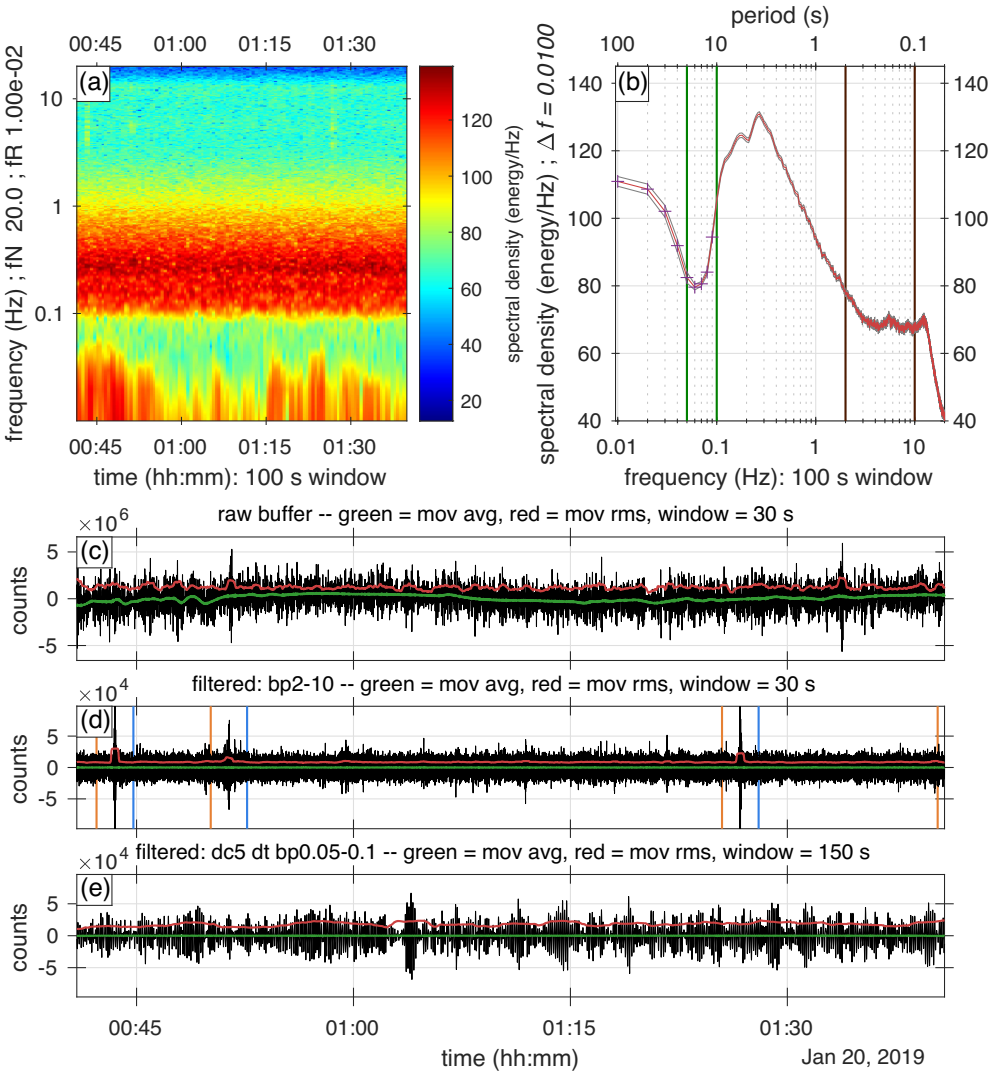

Figure A7. Another hour without transients (i.e. the hour before the event shown in Fig. 2 and Fig. A8), on a logarithmic frequency scale, for comparison with Fig. A6. Layout and labelling as in Fig. A1.

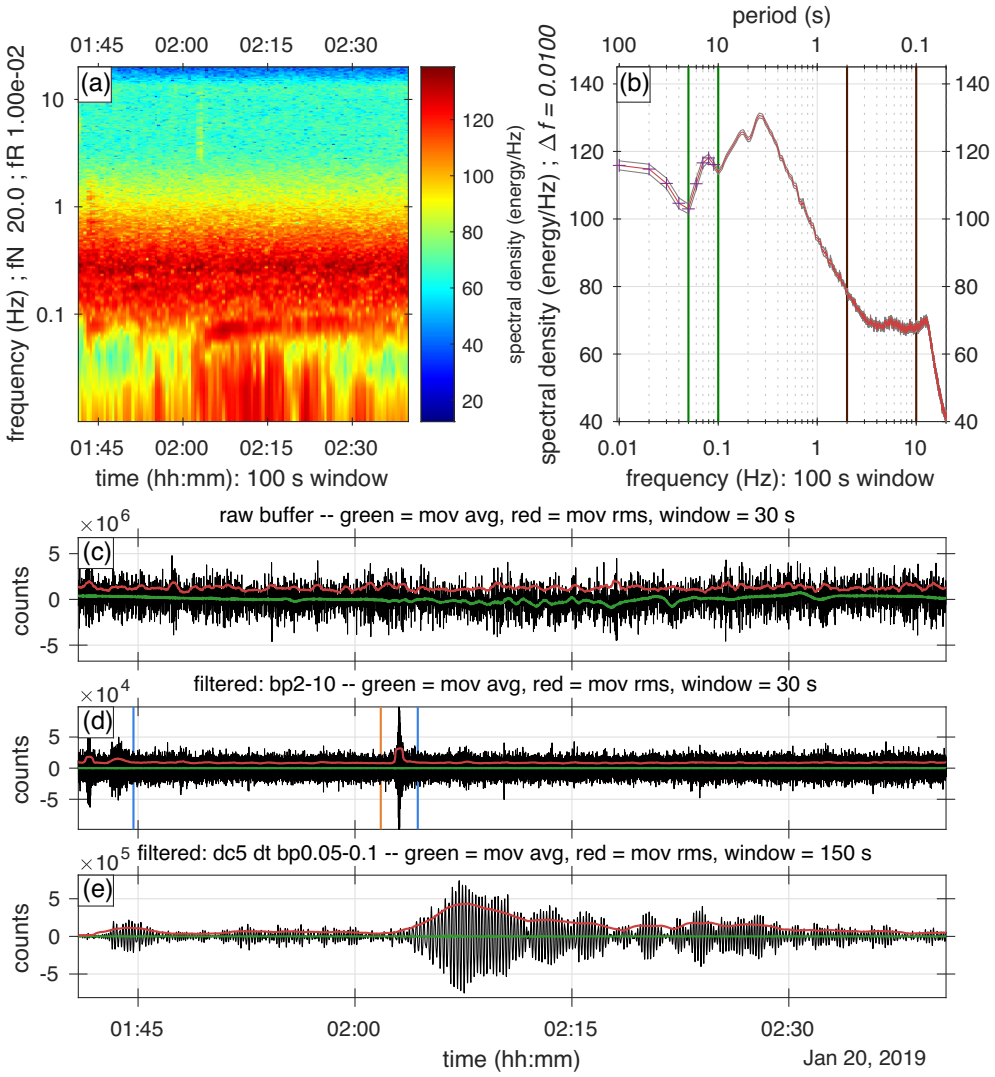

Figure A8. Another version of the event shown in Fig. 2, now drawn without the background noise curve. Layout and labelling as in Fig. A1.

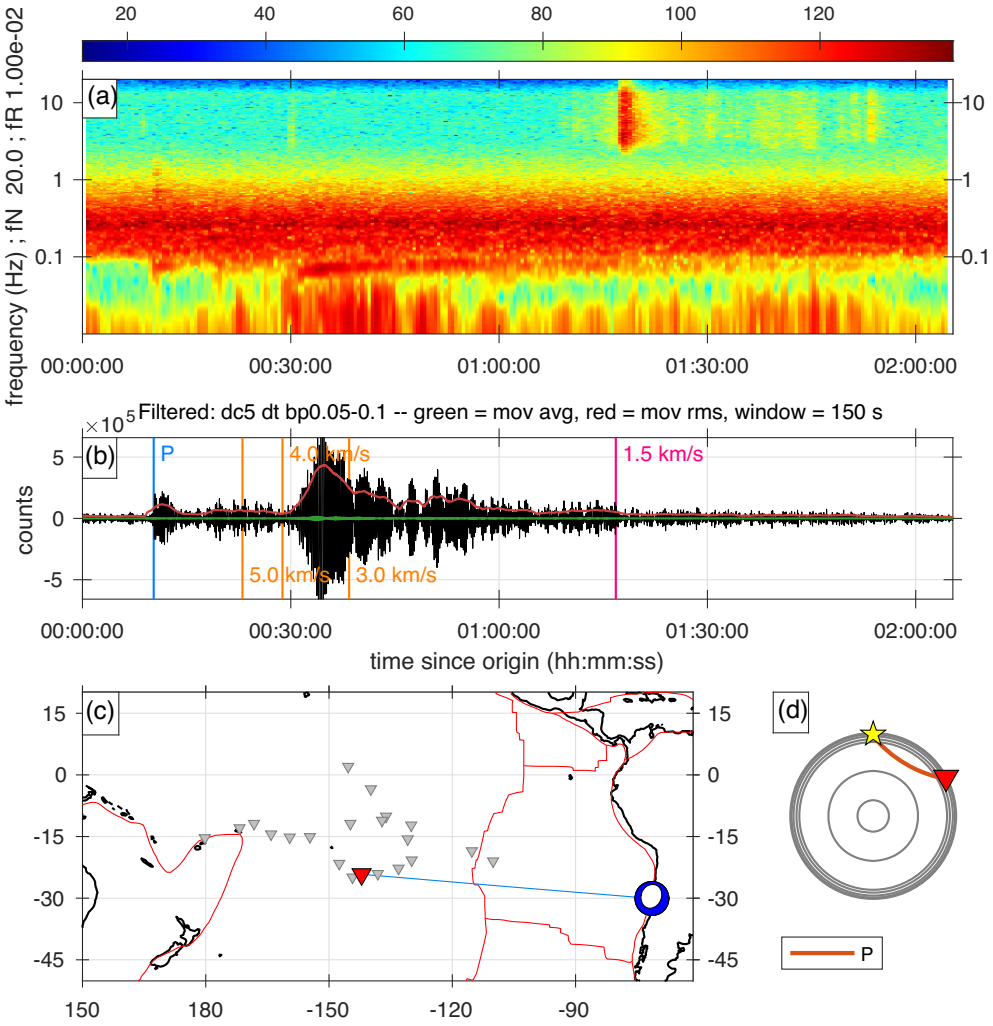

Figure A9. The full record of the signature earthquake Fig. 2, for comparison with Figs 3 and 4.